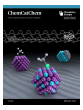

Carbon-Supported Bimetallic Ruthenium-Iridium Catalysts for Selective and Stable Hydrodebromination of Dibromomethane

Ali J. Saadun,[a] Sharon Mitchell,[a] Hristo Bonchev,[a] and Javier Pérez-Ramírez*[a]

Catalysts based on individual precious metals on carbon- and oxide-based carriers have shown remarkably selective behavior in the hydrodebromination of CH_2Br_2 to CH_3Br, an important transformation within halogen-mediated methane upgrading processes. However, the high susceptibility of the active phase to coking and to sintering, which cannot be overcome by controlling the nuclearity of the metal species, hinders their practical implementation. Herein, a platform of carbon-supported Ir–Ru catalysts with distinct metal ratios at comparable metal nanoparticle size (ca. 1.0 nm) was adopted to systematically study the effects of a second metal on reactivity and stability. Catalytic tests reveal ruthenium-doped iridium nanoparticles as the first system that combines high CH_3Br selectivity (up to 93%) with unprecedented stability, outperforming any of the previously reported catalysts. This superior performance was rationalized by the intimate interaction between the two metals, forming ruthenium-poor surface alloys, which enable suppressing deactivation mechanisms as well as over hydrogenation/coking pathways.

Heterogeneously-catalyzed selective hydrogenations find application in numerous industrial processes for the production of commodities, fine chemicals, and pharmaceuticals.[1] Often carried out over supported precious metals, these reactions are a prime example on how catalyst nanostructure impacts performance.[2] The structure sensitivity of the active phase has often been investigated by engineering its size and/or shape at the nanoscale.[3] Particularly the development and application of single atom catalysts (SACs), which contain spatially isolated atoms, received considerable attention.[4] Their high degree of metal dispersion, uniformity of the active sites, and tunable electronic properties grants unique catalytic performance, especially in terms of enhanced selectivity by limiting over hydrogenation and coking pathways, and enabled the exploration of nuclearity trends in diverse transformations.[5] Nevertheless, comparative studies indicate that the stability of SACs upon exposure to the reaction conditions is application dependent, preventing their universal employment.[6]

An example of practical relevance is the hydrodebromination of dibromomethane (CH_2Br_2) into methyl bromide (CH_3Br, Figure 1a), a key process in the context of bromine-mediated natural gas upgrading for the production of chemicals and fuels.[7] This reaction has mainly been studied over catalysts based on individual metals, initially reporting SiO_2-supported ruthenium nanoparticles as the only system selective to CH_3Br (up to 96%).[7] Nonetheless, fouling due to coking rapidly limits the wide application of the Ru-based catalysts.[7a] Interestingly, the stability of SiO_2-supported nanoparticles was found to be dependent on the active phase metal, decreasing in the order $Ir \approx Pt > Ni \approx Ru \approx Rh \gg Ag \approx Cu \approx Co \approx Fe$.[7a] Of these systems, only iridium and platinum displayed reasonably stable operation, whereas the other metals failed to preserve their initial activity. The stability of platinum and iridium nanoparticles, which mainly generate CH_4 (>47% selectivity), initiated further investigations aiming to improve the selectivity while maintaining the high durability of these metals. A recent study systematically assessed the effect of various platinum nanostructures supported on activated- (AC) or nitrogen-doped (NC) carbon, to assess metal size and host effects on performance.[5a] Whereas the unparalleled selectivity to CH_3Br (<98%) over the NC-supported platinum single atoms was reported, catalyst deactivation remained a major concern. Exposure to relevant hydrodebromination conditions ($T = 523$ K, $P = 1$ bar, $H_2:CH_2Br_2 = 4:1$) promotes agglomeration of the single atoms into nanoparticles and fouling due to coking, enhanced by the insufficient durability of the NC carrier. On the other hand, while carbon-supported nanoparticles generate a significant amount of CH_4 (>30% selectivity), they display greater retention of their performance regardless of the carrier/support properties (Table S1).[5b]

Consequently, the development of stable hydrodebromination metal catalysts that also integrate a high density of active and selective nanostructures remains of great interest. A possible strategy is the application of multimetallic nanoparticles, which have proven beneficial in various hydrogenations.[8] Specifically, bimetallic catalysts have generally provided better stability than monometallic systems in hydrodehalogenation reactions,[9] though their performance in CH_2Br_2 hydrodebromination has not been reported so far.

[a] A. J. Saadun, Dr. S. Mitchell, H. Bonchev, Prof. J. Pérez-Ramírez
Institute of Chemical and Bioengineering
Department of Chemistry and Applied Biosciences
ETH Zurich
Vladimir-Prelog-Weg 1
8093 Zurich (Switzerland)
E-mail: jpr@chem.ethz.ch

Supporting information for this article is available on the WWW under https://doi.org/10.1002/cctc.202101494

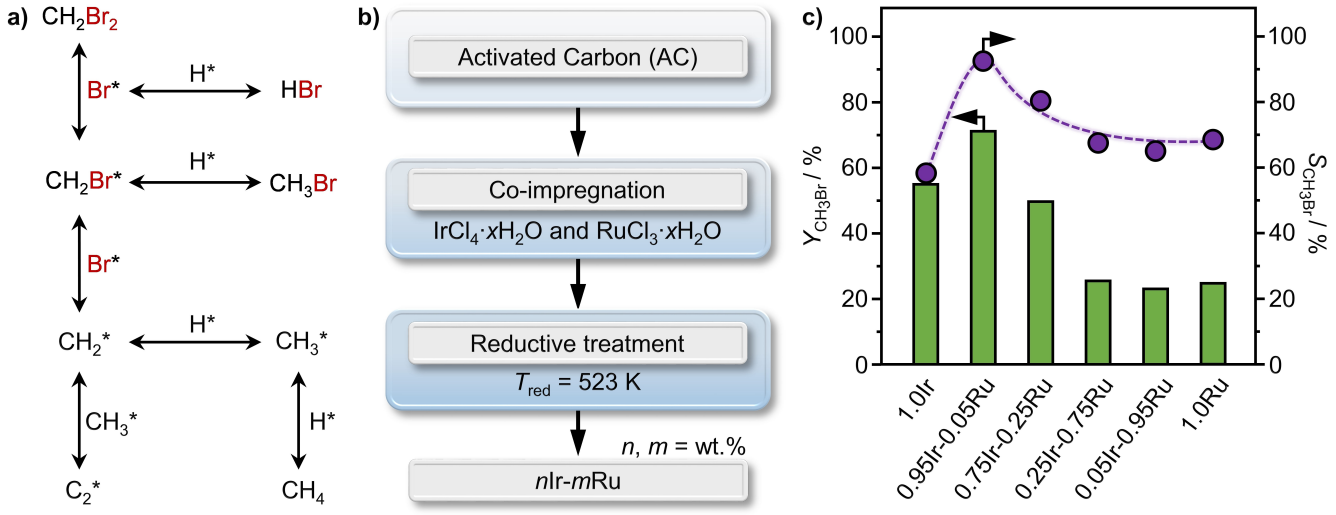

Figure 1. a) Reaction network of CH_2Br_2 hydrodebromination showing the pathways leading to CH_3Br, CH_4, and coke. b) Synthetic route for the preparation of the carbon-supported Ir–Ru bimetallic catalysts. c) Reactivity expressed as the yield to CH_3Br and product selectivity in CH_2Br_2 hydrodebromination over the catalysts. The activity was assessed at a constant space velocity of $F_T:W_{cat} = 70\ cm^3\ min^{-1}\ g_{cat}^{-1}$ while product selectivities were determined at *ca.* 20% CH_2Br_2 conversion achieved by adjusting the space velocity in the range of $F_T:W_{ca} = 150–350\ cm^3\ min^{-1}\ g_{cat}^{-1}$. Other reaction conditions: $CH_2Br_2:H_2:Ar:He = 6:24:5:65$, $T = 523$ K, $P = 1$ bar, and $tos = 15$ min.

Herein, potential cooperative effects between selective ruthenium and stable iridium-based systems are studied with the aim to develop a hydrodebromination catalyst that combines high reactivity with stability. For this purpose, a platform of AC-supported Ir–Ru systems with equivalent total metal loading of 1.0 wt% and varying Ir:Ru ratio (1.0:0, 0.95:0.05, 0.75:0.25, 0.25:0.75, 0.05:0.95, and 0:1.0) was prepared using a facile co-impregnation protocol followed by a reductive treatment at elevated temperatures (Figure 1b, see the Supporting Information for full synthesis details). The resulting AC-supported catalysts were denoted *n*Ir-*m*Ru, where *n* and *m* stand for the metal loading (in wt%). The Ir, Ru, as well as the total metal loading are close to the targeted values (Table S2). Analysis of the porous properties by N_2-sorption shows that the specific surface areas (S_{BET}, 1337–1408 $m^2\ g^{-1}$) and pore volumes (V_{pore}, 0.78–0.83 $cm^3\ g^{-1}$) were very similar.

These catalysts were evaluated in CH_2Br_2 hydrodebromination under optimized reaction conditions (Figure 1c). Interestingly, the CH_3Br selectivity evidenced at *ca.* 20% CH_2Br_2 conversion was found to be markedly affected by the Ir:Ru ratio (Figure 1c, Figure S1). It follows a volcano-type shape with the lowest values for 1.0Ir (58%), increasing to an exceptional 93% over 0.95Ir–0.05Ru, and dropping to *ca.* 70% at higher Ru contents. The only side product over 0.95Ir–0.05Ru is CH_4 (*ca.* 7%), which is significantly lower than the *ca.* 20% attained over the monometallic Ir-based counterpart. In line with previous reports, catalysts with high Ru-content display a high propensity to coke (up to 35%).[7a] Furthermore, the CH_3Br yield displays a similar trend as the selectivity, with the Ru-based catalysts showing the lowest yield (Figure 1c).

Analysis by scanning transmission electron microscopy in high-angle annular dark-field mode (HAADF-STEM) highlighted the abundance and uniform dispersion of metal nanoparticles across the support. The average diameter (centered around 1 nm) and morphology of metal nanoparticles in the catalysts were comparable (Figures 2a, S2, S3), indicating that their different performance did not originate from distinctions in size or shape. Energy-dispersive X-ray spectroscopy (EDX) maps of the elemental distribution of iridium and ruthenium in the high-performing samples (0.95Ir–0.05Ru, 0.75Ir–0.25Ru) evidence a close interaction between the two metals, showing their coexistence within the largest nanoparticles present. Despite the low ruthenium content in 0.95Ir-0.05Ru, a signal from the metal could be clearly detected. High-resolution transmission electron microscopy (HRTEM) images evidence the presence of crystalline nanoparticles. The observed lattice spacings of 2.30 Å and 2.17 Å are close to that expected for the Ir(111) plane of 2.20 Å (Figure 2a). The deviations could result from the alloying with Ru, but may also be due to the small size of the nanoparticles. In contrast, no reflections or any metal phase were observed in the X-ray diffraction (XRD) patterns of the catalysts, reflecting the small particle size and relatively low metal contents in the samples.

Further evidence for the formation of Ir–Ru alloys comes from analysis by the temperature-programmed reduction with hydrogen (H_2-TPR). Three distinctive types of profile are observed that can be grouped as (*i*) 1.0Ir, (*ii*) 0.95Ir–0.05Ru and 0.75Ir–0.25Ru, and (*iii*) the catalysts with higher Ru content, including 1.0Ru (Figure 2b). In particular, the high performing 0.95Ir–0.05Ru and 0.75Ir–0.25Ru catalysts exhibit a low-temperature reduction peak at *ca.* 360 K, which is distinct from the behavior observed for the monometallic systems, where the first reduction peaks are observed at 460 K (Ir) or 400 K (Ru). Such a shift has previously been associated with hydrogen spillover between the two metals, indicating that they are in close proximity.[10a,b] This is also supported by the fact that H_2-

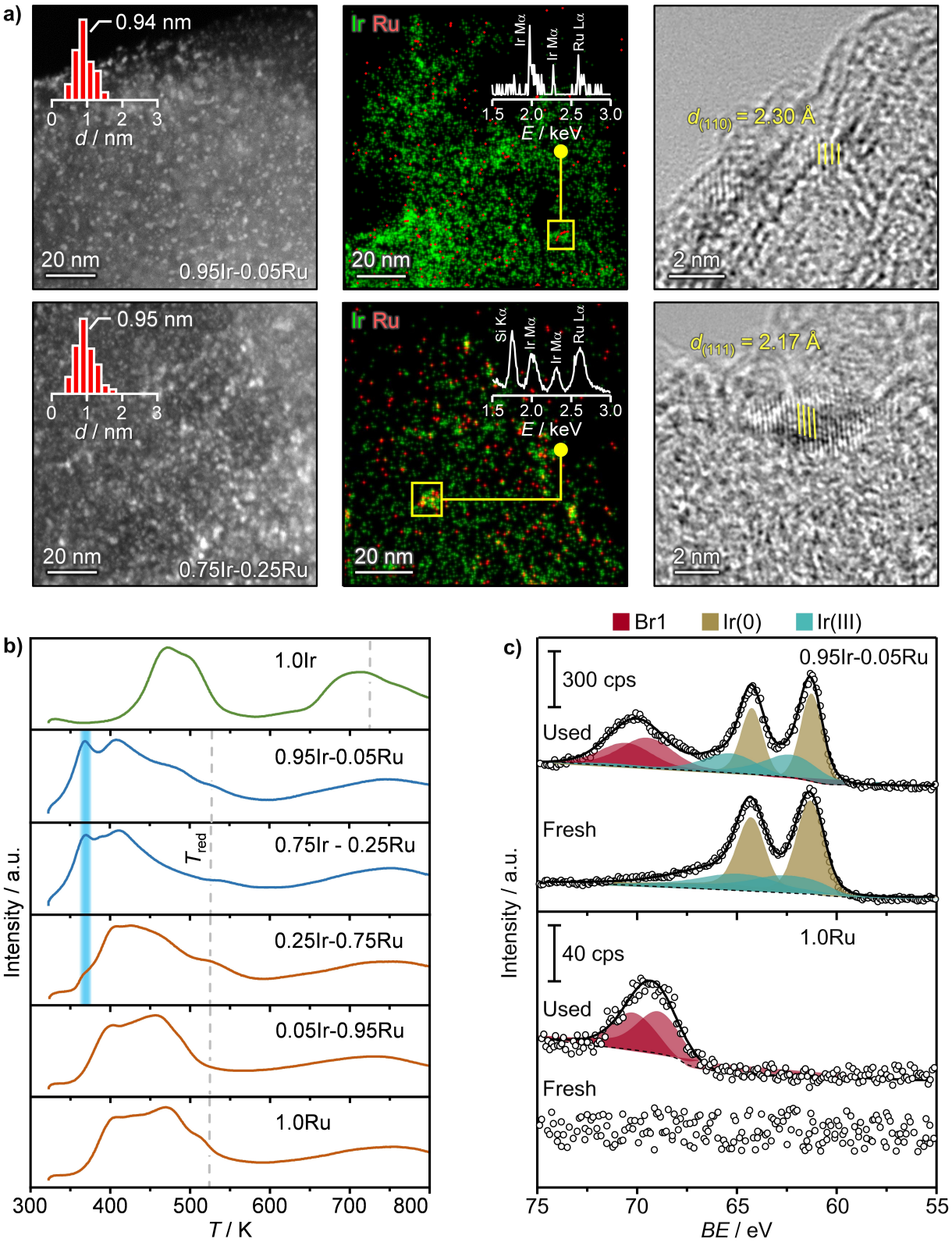

Figure 2. a) HAADF-STEM micrographs with particle size distributions (inset), EDX elemental maps with spectra corresponding to the areas marked (inset), and HRTEM images of selected catalysts in fresh form. b) H_2-TPR profiles of the catalyst precursors with the temperature of the reductive treatment, T_{red}, indicated by the vertical dashed lines and c) Ir 4*f* XPS spectra of selected catalysts in fresh form and after 10 h in CH_2Br_2 hydrodebromination. The dark gray lines and open circles represent the overall fit and the raw data, respectively, while the colored areas indicate the fit of distinct chemical components. Reaction conditions as specified in the caption of Figure 1.

TPR profiles of 0.95Ir–0.05Ru and 0.75Ir–0.25Ru are not simply the sum of the corresponding monometallic profiles.[10c] In contrast, the profiles of 0.25Ir–0.75Ru, 0.05Ir–0.95Ru, and 1.0Ru are very comparable, consistent with their similar catalytic performance, suggesting that unalloyed Ru-phases dominate the surface properties.[10b]

In agreement with the expected electronic properties of the metal alloy nanoparticles, X-ray photoelectron spectroscopy (XPS) analysis confirms dominant contributions centered at 61.1 and 461.3 eV, characteristic of metallic Ir and Ru phases, respectively (Figures 2c, S6). A small fraction of oxidized metal species is also visible, as commonly observed for supported nanoparticles of similar size and typically attributed to a strong metal-support interaction.

The catalysts were further assessed in 10 h stability tests with an initial CH_2Br_2 conversion of *ca.* 20% (Figure 3). Consistent with previous studies, monometallic Ir and Ru display contrasting performance with the former showing a relatively stable behavior. For the bimetallic systems, the rate of activity loss correlates with the Ru content. Strikingly, the 0.95Ir 0.05Ru catalyst preserves its highly selective performance and displays a stability comparable with that of the monometallic system (1.0Ir). Characterization of the used catalysts by N_2-sorption, XRD, HAADF STEM, and XPS revealed that both coke deposition and, to a lesser extent, bromination contribute to catalyst deactivation. The HAADF-STEM micrographs of the monometallic systems indicate slight active phase sintering (Figure S2). In contrast, the bimetallic catalysts preserve their structure, with no visible change in average particle diameter or morphology, and similar uniform distributions of the component metals (Figures S5, S4). This suggests that alloying reduces the mobility of the metal nanoparticles, thereby increasing durability. XPS indicated the presence of Br-species on the surface of used catalysts (Figure 2c), though the majority is believed to be bound to the carbon-support since the XPS contributions of oxidized Ir and Ru species did not change significantly (Figures 2c, S6). Further insights were gained by conducting kinetic analysis over representative systems, showing comparable activation energies between 1.0Ir and 0.95Ir–0.05Ru of 44 and 41 kJ mol^{-1}, respectively (Figure 4a), lower than that attained over 1.0Ru (58 kJ mol^{-1}). Furthermore, the normalized reaction rate increases *ca.* 4.5 times over 1.0Ir upon increasing the H_2 partial pressure from 6 to 72 kPa (Figure 4b). Comparatively, the increase was lower over 0.95Ir–0.05Ru (4 times) or 1.0Ru (3.8 times). With a derived partial order in H_2 of 0.73, 0.95Ir–0.05Ru falls between the values of the monometallic systems (0.81 and 0.64 for 1.0Ir and 1.0Ru, respectively). This value is lower than the orders obtained over monometallic catalysts that display a high propensity to CH_4 (usually > 0.8).[2a,7a] These systems display facile H_2 activation, leading to a high surface coverage by H-atoms that readily react with carbon-containing species. The kinetic fingerprints of 0.95Ir–0.05Ru suggest that electronic effects due to alloying play an important role in moderating the presence of surface H-atoms (Figure 5), thereby limiting overhydrogenation pathways. As previously disclosed, a small change in the adsorption energy of key intermediates could invoke a dramatic change in the selectivity behavior of metal nanoparticles in CH_2Br_2 hydrodebromination.[7a]

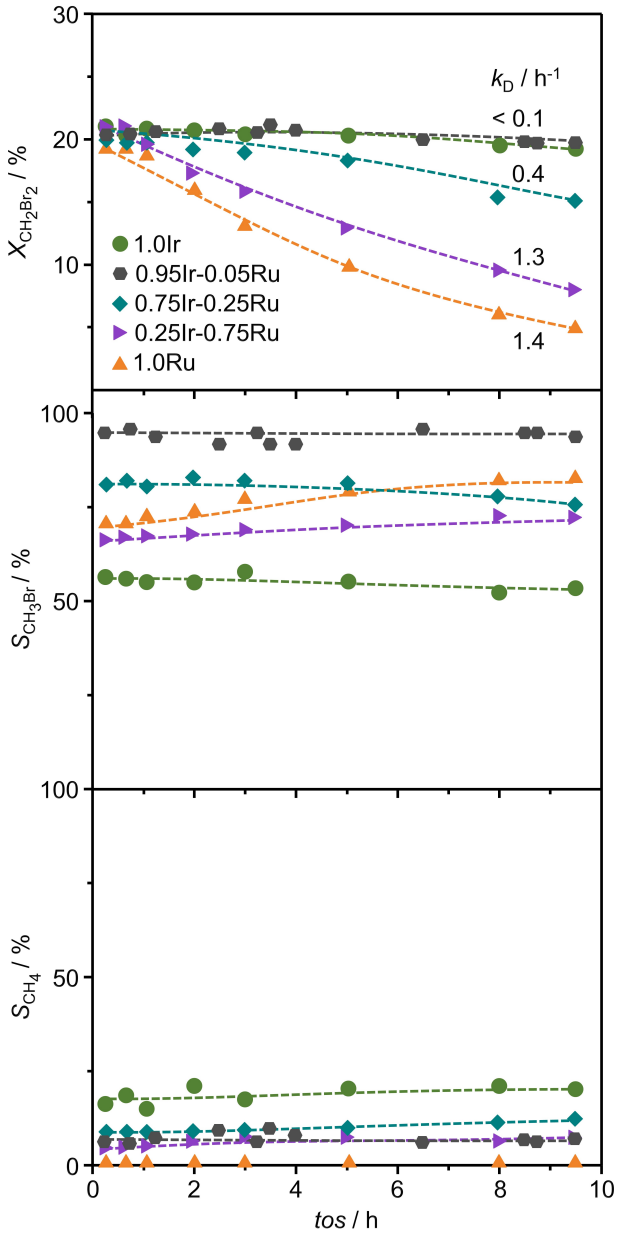

Figure 3. Time-on-stream (*tos*) performance of the catalysts. The deactivation constant, k_D, was derived *via* a simple linear regression of the full data range. Reaction conditions as specified in the caption of Figure 1. *X* and *S* stand for conversion and selectivity of the indicated compound, respectively.

The limited propensity to form coke and the high stability over 0.95Ir–0.05Ru suggests that the majority of the Ru-atoms are highly dispersed over the nanoparticle. Combined with distinct behavior evidenced by H_2-TPR, the close proximity of the metals observed by EDX mapping, and the predominantly metallic character shown by XPS, this suggests the possible formation of a single-atom alloy (Figure 5). With increasing Ru content, more coke is generated and the catalyst stability decreases, likely due to the formation of larger Ru domains. With high Ru-loadings, the comparable properties to the

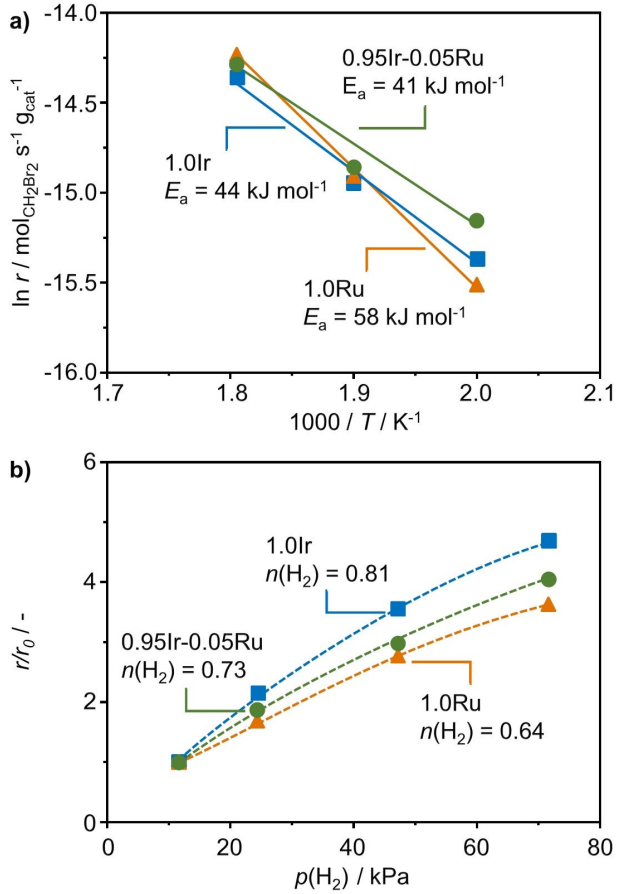

Figure 4. Rate of CH_2Br_2 hydrodebromination of selected catalysts as a function of a) temperature and b) inlet partial pressure of H_2. Each catalytic data point was gathered using materials in fresh form. Reaction conditions: a) CH_2Br_2:H_2:Ar:He = 6:24:5:65, F_T:W_{cat} = 50–600 cm^3 min^{-1} g$_{cat}^{-1}$, T = 498–548 K; b) CH_2Br_2:H_2:Ar:He = 6:6–72:5:17–83, F_T:W_{cat} = 50–700 cm^3 min^{-1} g$_{cat}^{-1}$, T = 523 K. All tests were conducted at P = 1 bar and *tos* = 15 min.

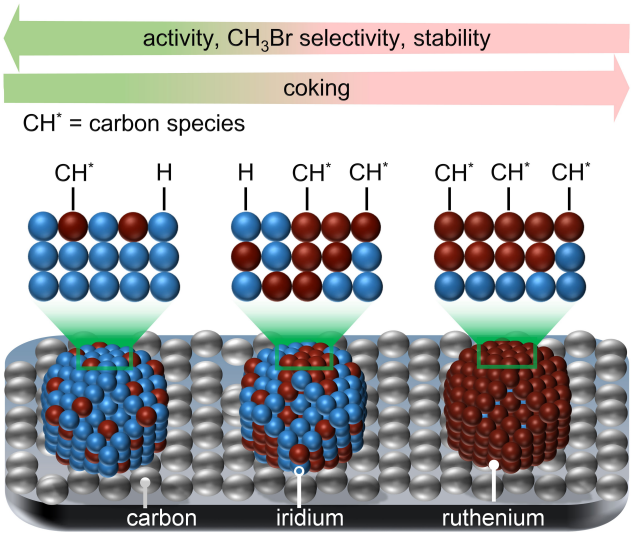

Figure 5. Possible scheme of Ir-Ru mixing effects on activity, selectivity, and stability in CH_2Br_2 hydrodebromination. A likely metal surface occupation by CH- and H-species during reaction is presented (middle). Green areas (top) indicate optimal catalytic performance.

monometallic Ru system point to the formation of Ru-rich nanoparticle surfaces. Nevertheless, with existing techniques the precise characterization of the nanostructure of these catalysts remains challenging, particularly due to the small size of the nanoparticles present and the low Ru content in the best-performing catalyst.

In conclusion, we have demonstrated the exceptional CH_2Br_2 hydrodebromination performance of ruthenium-doped Ir nanoparticles on carbon, for the first time combining high CH_3Br selectivity with unparalleled stability. Coking and active phase sintering, pathways responsible for the deactivation of state-of-the-art catalysts, are suppressed by exploiting synergetic effects in this bimetallic system. Further, by preparing a platform of Ir–Ru catalysts with distinct metal ratios at comparable metal nanoparticle size and porous properties, we performed a systematic study to link alloy structures and properties with performance. While monometallic Ir-based catalysts are robust, they generate considerable amounts of side products. Doping of Ir with Ru significantly improves its CH_3Br selectivity (93%) and maintains the high stability, thus outperforming benchmark Ru nanoparticles. A close interaction between the two metals, forming Ru-poor surface alloys, was found to be crucial in suppressing over hydrogenation and coking pathways, which reduce selectivity to the target CH_3Br. The improved performance of the Ir-Ru catalytic system was further rationalized based on the interplay between Ir and Ru, which alters the interaction with H_2 compared to the monometallic catalysts as evidenced by the kinetic fingerprints. These findings demonstrate that the development of multimetallic nanostructures can serve as an effective strategy for generating hydrodebromination catalysts that combine high reactivity and stability.

Experimental Section

Full experimental details, additional characterization and catalytic data are provided as Supporting Information.

Acknowledgements

This work was supported by ETH research grant ETH-43 18-1 and NCCR Catalysis, a National Centre of Competence in Research funded by the Swiss National Science Foundation. The authors thank the Scientific Center for Optical and Electron Microscopy, ScopeM, and the Swiss Federal Laboratories for Materials Science and Technology, EMPA, for access to their facilities. We thank Simon Büchele for conducting XPS analyses. Open access funding provided by Eidgenossische Technische Hochschule Zurich.

Conflict of Interest

The authors declare no conflict of interest.

Keywords: bimetallic catalysts · hydrodebromination · iridium · nanoparticles · ruthenium

[1] a) C. H. Bartholomew, R. J. Farrauto, *Fundamentals of Industrial Catalytic Processes*, John Wiley & Sons, **2011**; b) S. Nishimura, *Handbook of Heterogeneous Catalytic Hydrogenation for Organic Synthesis*, Wiley New York, **2001**; c) S. Kattel, P. Liu, J. G. Chen, *J. Am. Chem. Soc.* **2017**, *139*, 9739–9754; d) I. Staffell, D. Scamman, A. V. Abad, P. Balcombe, P. E. Dodds, P. Ekins, N. Shah, K. R. Ward, *Energy Environ. Sci.* **2019**, *12*, 463–491.

[2] a) A. J. Saadun, G. Zichittella, V. Paunović, B. A. Markaide-Aiastui, S. Mitchell, J. Pérez-Ramírez, *ACS Catal.* **2020**, *10*, 528–542; b) L. Zhang, M. Zhou, A. Wang, T. Zhang, *Chem. Rev.* **2019**, *120*, 683–733; c) N. R. Shiju, V. V. Guliants, *Appl. Catal. A* **2009**, *356*, 1–17; d) S. Mitchell, R. Qin, N. Zheng, J. Pérez-Ramírez, *Nat. Nanotechnol.* **2021**, *16*, 129–139; e) G. Vilé, D. Albani, N. Almora-Barrios, N. López, J. Pérez-Ramírez, *ChemCatChem* **2016**, *8*, 21–33.

[3] a) F. Zaera, *ACS Catal.* **2017**, *7*, 4947–4967; b) L. Liu, A. Corma, *Chem. Rev.* **2018**, *118*, 4981–5079; c) P. Mäki-Arvela, J. Hájek, T. Salmi, D. Y. Murzin, *Appl. Catal. A* **2005**, *292*, 1–49; d) I. Lee, F. Delbecq, R. Morales, M. A. Albiter, F. Zaera, *Nat. Mater.* **2009**, *8*, 132.

[4] a) S. K. Kaiser, Z. Chen, D. Faust Akl, S. Mitchell, J. Pérez-Ramírez, *Chem. Rev.* **2020**, *120*, 11703–11809; b) X.-F. Yang, A. Wang, B. Qiao, J. Li, J. Liu, T. Zhang, *Acc. Chem. Res.* **2013**, *46*, 1740–1748; c) F. Zhang, Y. Zhu, Q. Lin, L. Zhang, X. Zhang, H. Wang, *Energy Environ. Sci.* **2021**, *14*, 2954-3009 ; d) A. Wang, J. Li, T. Zhang, *Nat. Chem. Rev.* **2018**, *2*, 65–81; e) J. Liu, *ACS Catal.* **2017**, *7*, 34–59; f) X. Cui, W. Li, P. Ryabchuk, K. Junge, M. Beller, *Nat. Catal.* **2018**, *1*, 385–397; g) F. R. Lucci, J. Liu, M. D. Marcinkowski, M. Yang, L. F. Allard, M. Flytzani-Stephanopoulos, E. C. H. Sykes, *Nat. Commun.* **2015**, *6*, 8550.

[5] a) A. J. Saadun, S. K. Kaiser, A. Ruiz-Ferrando, S. Pablo-García, S. Büchele, E. Fako, N. López, J. Pérez-Ramírez, *Small* **2021**, *17*, 2005234; b) A. J. Saadun, A. Ruiz-Ferrando, S. Büchele, D. Faust Akl, N. López, J. Pérez-Ramírez, *J. Catal.* **2021**, *404*, 291–305; c) S. K. Kaiser, R. Lin, F. Krumeich, O. V. Safonova, J. Pérez-Ramírez, *Angew. Chem. Int. Ed.* **2019**, *58*, 12297–12304. *Angew. Chem.* **2019**, *131*, 12425–12432; d) S. K. Kaiser, E. Fako, G. Manzocchi, F. Krumeich, R. Hauert, A. H. Clark, O. V. Safonova, N. López, J. Pérez-Ramírez, *Nat. Catal.* **2020**, *3*, 376–385.

[6] a) S. Mitchell, J. Pérez-Ramírez, *Nat. Commun.* **2020**, *11*, 1–3; b) S. Mitchell, E. Vorobyeva, J. Pérez-Ramírez, *Angew. Chem. Int. Ed.* **2018**, *57*, 15316–15329. *Angew. Chem.* **2018**, *130*, 15538–15552.

[7] a) A. J. Saadun, S. Pablo-García, V. Paunović, Q. Li, A. Sabadel-Rendón, K. Kleemann, F. Krumeich, N. López, J. Pérez-Ramírez, *ACS Catal.* **2020**, *10*, 6129–6143; b) G. Zichittella, J. Pérez-Ramírez, *Chem. Soc. Rev.* **2021**, *50*, 2984–3012; c) R. Lin, A. P. Amrute, J. Pérez-Ramírez, *Chem. Rev.* **2017**, *117*, 4182–4247; d) K. Ding, A. R. Derk, A. Zhang, Z. Hu, P. Stoimenov, G. D. Stucky, H. Metiu, E. W. McFarland, *ACS Catal.* **2012**, *2*, 479–486.

[8] a) S. Matsuda, S. Masuda, S. Takano, N. Ichikuni, T. Tsukuda, *ACS Catal.* **2021**, *11*, 10502–10507; b) T. Chen, V. O. Rodionov, *ACS Catal.* **2016**, *6*, 4025–4033; c) P. Buchwalter, J. Rose, P. Braunstein, *Chem. Rev.* **2015**, *115*, 28–126; d) M. Sankar, N. Dimitratos, P. J. Miedziak, P. P. Wells, C. J. Kiely, G. J. Hutchings, *Chem. Soc. Rev.* **2012**, *41*, 8099–8139.

[9] a) S. R. Lee, J. M. Cho, M. Son, M.-J. Park, W. Y. Kim, S. Y. Kim, J. W. Bae, *Chem. Eng. J.* **2018**, *331*, 556–569; b) M. Bonarowska, K. Matus, A. Śrębowata, J. Sá, *Sci. Total Environ.* **2018**, *644*, 287–297; c) M. Martin-Martinez, L. M. Gómez-Sainero, J. Bedia, A. Arevalo-Bastante, J. J. Rodriguez, *Appl. Catal. B* **2016**, *184*, 55–63; d) S. Liu, J. A. Otero, M. Martin-Martinez, D. Rodriguez-Franco, J. J. Rodriguez, L. M. Gómez-Sainero, *Catalysts* **2020**, *10*, 1462.

[10] a) S. Xu, S. Shen, Z. Wei, S. Zhao, L. Zuo, M. Chen, L. Wang, Y. Ding, P. Chen, S. Chu, Y. Lin, K. Qian, H. Liang, *Nano Res.* **2020**, *13*, 2735–2740; b) A. Wong, Q. Liu, S. Griffin, A. Nicholls, J. R. Regalbuto, *Science* **2017**, *358*, 1427–1430; c) R. J. Chimentão, H. Oliva, V. Russo, J. Llorca, J. L. G. Fierro, P. Mäki-Arvela, D. Y. Murzin, D. Ruiz, *J. Phys. Chem. C* **2021**, *125*, 9657–9678.

Manuscript received: October 2, 2021
Revised manuscript received: November 11, 2021
Accepted manuscript online: November 15, 2021
Version of record online: November 29, 2021